Check for updates

ADVANCED MATERIALS
www.advmat.de

Understanding Effects of Alkyl Side-Chain Density on Polaron Formation Via Electrochemical Doping in Thiophene Polymers

*Katherine Stewart, Katia Pagano, Ellasia Tan, Matyas Daboczi, Martina Rimmele, Joel Luke, Salvador Eslava, and Ji-Seon Kim**

Polarons exist when charges are injected into organic semiconductors due to their strong coupling with the lattice phonons, significantly affecting electronic charge-transport properties. Understanding the formation and (de)localization of polarons is therefore critical for further developing organic semiconductors as a future electronics platform. However, there are very few studies reported in this area. In particular, there is no direct in situ monitoring of polaron formation and identification of its dependence on molecular structure and impact on electrical properties, limiting further advancement in organic electronics. Herein, how a minor modification of side-chain density in thiophene-based conjugated polymers affects the polaron formation via electrochemical doping, changing the polymers' electrical response to the surrounding dielectric environment for gas sensing, is demonstrated. It is found that the reduction in side-chain density results in a multistep polaron formation, leading to an initial formation of localized polarons in thiophene units without side chains. Reduced side-chain density also allows the formation of a high density of polarons with fewer polymer structural changes. More numerous but more localized polarons generate a stronger analyte response but without the selectivity between polar and nonpolar solvents, which is different from the more delocalized polarons that show clear selectivity. The results provide important molecular understanding and design rules for the polaron formation and its impact on electrical properties.

1. Introduction

The design of conjugated polymers for organic semiconducting device applications has been largely driven by the potential for alternative low-cost, solution-processable, and high-performance devices. There have been many advances in their functionality and applications, with the fields of organic light emitting diodes being the first to achieve widespread commercialization[1] and organic photovoltaics (OPV) heading toward commercial products.[2] One factor new device applications will need to consider is the molecular design of the conjugated polymer systems.[3] This is especially important for organic biosensors where high efficiencies are often achieved with no detailed investigation into understanding the sensing responses.[4] Understanding key relationships between molecular design and charge formation for device operation will be crucial for designing new high-performance materials.

A charge carrier in an organic semiconductor, known as a polaron, is a charge accompanied by a lattice distortion.[5] For example, a hole polaron is formed by the removal of an electron from the highest occupied molecular orbital (HOMO) creating a radical cation with localized electronic states within the bandgap.[6] This is very different to the band transport of inorganic semiconductors where delocalized waveforms are able to extend over the crystalline lattice.[7] During polaron formation in organic semiconductors, the lattice structural change results in a redistribution of π-electrons along the main conjugated backbone. The reorganization energy (RE) is the energy required to adapt to the electronic excitation, which limits the charge carrier injection and mobility.[8] Polarons are unable to move freely as they are strongly coupled to the electronic and geometric features of the conjugated polymer, which is known as electron–phonon coupling.[9,10] Polaron delocalization is therefore strongly linked to the structural properties of a conjugated polymer chain, can spread over several units, and is highly dependent on chemical structure, conformation, and thin film microstructure.[11,12] When designing a charge-transport layer, understanding how the polymer structure affects polaron formation is important for

K. Stewart, K. Pagano, E. Tan, J. Luke, J.-S. Kim
Department of Physics and Centre for Processable Electronics
Imperial College London
London SW7 2AZ, UK
E-mail: ji-seon.kim@imperial.ac.uk
M. Daboczi, S. Eslava
Department of Chemical Engineering and Centre for Processable Electronics
Imperial College London
London SW7 2AZ, UK
M. Rimmele
Department of Chemistry and Centre for Processable Electronics
Imperial College London
London W12 0BZ, UK

The ORCID identification number(s) for the author(s) of this article can be found under https://doi.org/10.1002/adma.202211184

© 2023 The Authors. Advanced Materials published by Wiley-VCH GmbH. This is an open access article under the terms of the Creative Commons Attribution License, which permits use, distribution and reproduction in any medium, provided the original work is properly cited.

DOI: 10.1002/adma.202211184

optimizing charge transport; and hence, device performance. Therefore, a detailed study on various conjugated polymers and the critical properties for efficient polaron formation is required.

Previous work has demonstrated the potential of solid-state ionic liquids blended with conjugated polymers as highly sensitive and selective sensors. The specific properties of the ionic liquid have been explored, revealing the advantage of the solid-state semi crystalline nature of $[C_1C_{12}IM^+][PF_6^-]$ over amorphous ionic liquids.[13] The polymer properties were investigated in both a high mobility electron donor–electron acceptor (D–A) conjugated copolymer[14] and in the model homopolymer poly(3-hexylthiophene-2,5-diyl) (P3HT), with the importance of molecular weight and regioregularity being investigated.[15] Using this conjugated polymer:solid-state ionic liquid blend system, long-lived stable polarons in the solid-state are formed via electrochemical doping. Electrochemical doping describes a bias-driven doping of a semiconductor system with charge carrier generation that is facilitated by the surrounding ions.[16,17] Electrochemical doping is most commonly applied via an electrolyte-gate in an electrochemical cell where mobile ions are able to penetrate the organic semiconductor thin film resulting in an organic semiconductor layer containing both charge carriers and counter ions.[18] Here, we use a solid-state ionic liquid blended with the conjugated polymer in solution and cast as a single thin film which allows interactions between the immobile PF_6^- anion and the polymer backbone to generate more holes in the bulk film.[14] This solid-state electrochemical doping/dedoping process differs from chemical doping whereby there is no ground state doping, the doping interaction only occurs under bias and is reversible with the removal of the applied bias.

Here, we utilize the methods developed in the solid-state ionic liquid blend system to establish the effect of side-chain density on polaron formation in conjugated polymers. With the simple progression from homopolymer P3HT to poly(3,3‴-didodecyl quaterthiophene) (PQT12), where a less uniform backbone is created by reducing the side-chain density, we compare the nature of polaron formation in the two polymers. Step by step characterization of polarons as they form under real device conditions enables the study of the molecular structure-dependent polaron formation to understand the effect of side chain density.

P3HT is an ideal model polymer with extensive research in literature and many advantages in low-cost device applications, including solution processability and ready synthesis scalability, with excellent control over molecular weight (M_w) and regioregularity (RR).[19] PQT12 is also a thiophene-based polymer but with a reduced side-chain density introducing unsubstituted thiophene rings to the polymer backbone.[20] The lower side-chain density offers enhanced chain ordering and crystallinity,[21] allowing greater interdigitation of side chains on adjacent backbones and helping to promote the formation of highly ordered lamellae.[22] PQT12 was initially developed for use in field effect transistors and has since been applied to a variety of optoelectronic devices[23] including sensing applications as it is highly photosensitive and air stable.[23,24] Beyond the applications of P3HT and PQT12, thiophenes are the building blocks of a vast array of organic semiconducting polymers,[25] including as a common component of the donor unit of high performing D–A copolymers used in OPV, such as the diketopyrrolopyrrole (DPP) and isoindigo acceptor-based copolymers.[26,27]

By comparing these two polymers, which have significant similarities in the structure of the conjugated backbone, we aim to give a detailed insight into the importance of molecular design rules, such as side-chain density, on electrical characteristics. While previous studies have reported how the optical bandgap changes under polaron formation[28] or introduced strong chemical dopants to visualize polaron delocalization,[29,30] we directly probe the vibrational modes involved in polaron formation using reversible electrochemical doping under operational conditions. This novel technique enables the study of the individual vibrational modes involved in polaron formation and the resulting charge redistribution, allowing us to gain an understanding of the effect of side-chain density on the polaron formation pathway. We show that the reduction of side-chain density enables the formation of higher polaron density with less structural change to the conjugated polymer backbone. We then demonstrate how the mechanism of polaron formation is an important consideration in device applications by comparing the volatile organic compounds (VOC) sensing response of P3HT and PQT12.

2. Results and Discussion

To study the effect on side-chain density, we compared two thiophene-based conjugated polymers, P3HT and PQT12 (**Figure 1**a). P3HT is formed of a repeating backbone of thiophene rings with a hexyl alkyl chain on the 3-position. In regioregular P3HT, the monomeric unit is connected with predominantly head to tail linkages. PQT12 consists of the same thiophene backbone but the side-chain density is reduced to the first and last ring of a four-ring monomeric unit, and the side-chain length is increased to a dodecyl alkyl chain. Conjugated polymers were blended at a 1:1 ratio with solid-state ionic liquid, 1-dodecane-3-methylimidazolium hexafluorophosphate $[C_1C_{12}IM^+][PF_6^-]$, herein referred to as SSIL, to create a conjugated polymer:solid-state ionic liquid blend that overcomes the low conductivity of polymer only chemiresistors. It should be noted that in previous work, the molecular weight dependence of P3HT was shown to have a significant impact on the electrochemical performance of P3HT:SSIL.[15] Molecular weight studies with PQT12 are less common with PQT12 due to the step-growth nature of the polymerization and the limited commercial availability.[31,32] Therefore, in this study, comparison will focus on the optimum P3HT:SSIL blend (58 kg mol^{-1}) and PQT12 (14 kg mol^{-1}). Figure S1, Supporting Information, shows the comparison of PQT12 with a range of P3HT molecular weight, where the electrical performance of PQT12 has been matched with the high performing P3HT in order to compare the optimal electrochemical doping in each system.

2.1. Optical and Electrical Characterization

First, the optical properties of P3HT and PQT12 are compared in Figure 1c. For P3HT, the optical absorption maximum (λ_{max}) is centered at 540 nm with a bandgap of 1.9 eV, whilst PQT12 has a blueshifted λ_{max} at 520 nm and a larger optical bandgap of 2.0 eV. Upon the addition of SSIL, there is no increase in the sub-gap polaronic absorption band at 800 nm showing there is no

© 2023 The Authors. Advanced Materials published by Wiley-VCH GmbH

15214095, 2024, 20, Downloaded from https://onlinelibrary.wiley.com/doi/10.1002/adma.202211184 by Imperial College London, Wiley Online Library on [17/06/2024]. See the Terms and Conditions (https://onlinelibrary.wiley.com/terms-and-conditions) on Wiley Online Library for rules of use; OA articles are governed by the applicable Creative Commons License

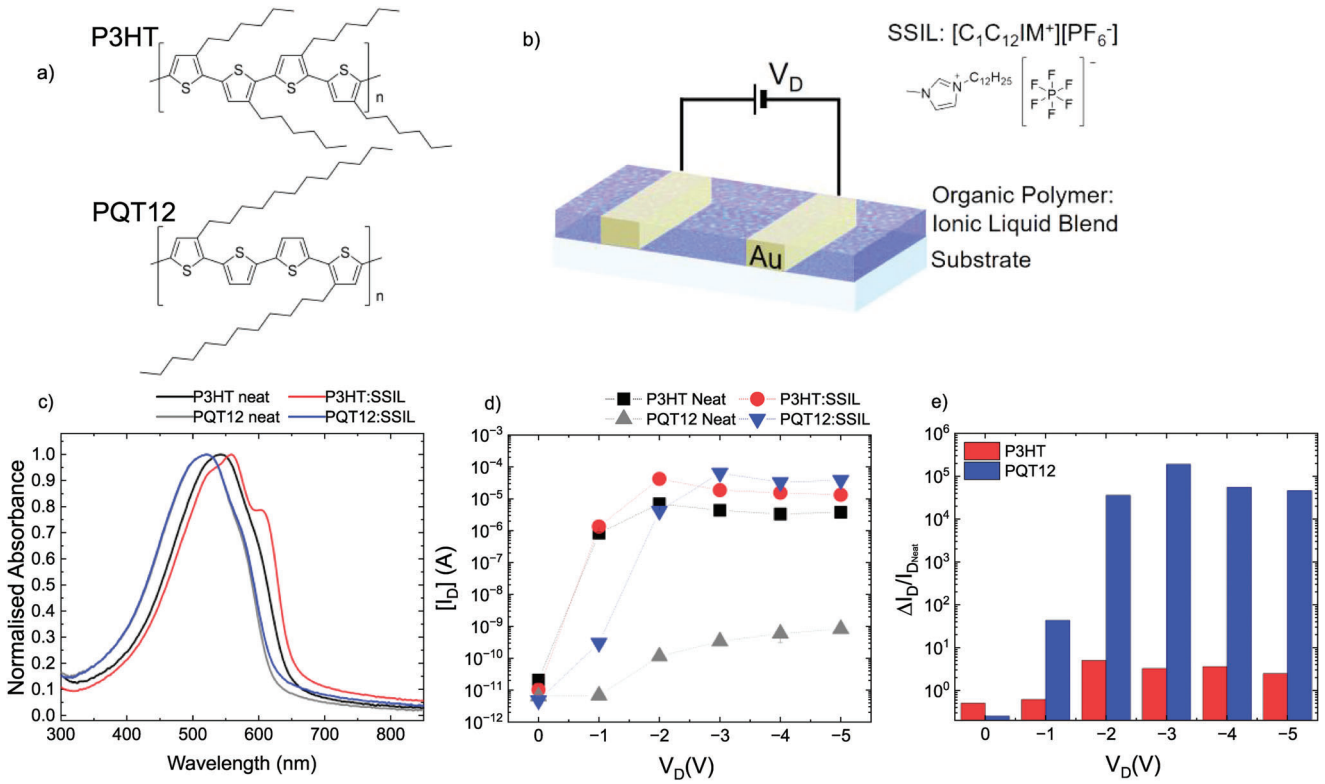


Figure 1. a) Chemical structures showing four monomer units of P3HT and a monomer of PQT12. b) Diagram of chemiresistor device structure used for organic polymer:ionic liquid blend characterization with ionic liquid structure (SSIL) $[C_1C_{12}IM^+][PF_6^-]$. c) Normalized absorbance spectra of P3HT neat, P3HT:SSIL, PQT12 neat, and PQT12:SSIL. d) Driven voltage dependence and e) the fractional change in driven voltage dependence from neat to blend across $L = 5$ µm, $W = 2$ mm chemiresistor channel.

ground state doping.[33] This confirms SSIL does not chemically dope either of the conjugated polymers. In P3HT:SSIL, there is a significant increase in the shoulder at 600 nm showing that the SSIL increases the order of packing in P3HT.[34] In contrast, there is no change to peak position or shape for the PQT12:SSIL blend.

The electrical performance was compared using an applied voltage dependence in chemiresistor devices (Figure 1b). A constant voltage is applied between source and drain electrodes and the current measured. A chemiresistor is a simple resistive device operating in the bulk conductivity regime so an increase in current at a given voltage is indicative of an increase in conductivity.[35] Figure 1d shows the mean drain current (I_D) measured for a series of applied voltages. Neat P3HT has a relatively high bulk conductivity for a semiconducting polymer measuring an I_D of 7 µA at an applied voltage of $V_D = -2$ V. In contrast, neat PQT12 measures a very low driven voltage dependence, $I_D = 0.001$ µA, showing that the bulk conductivity is much lower than neat P3HT. There are a number of factors contributing to the difference in driven voltage dependence of P3HT and PQT12; the lower conductivity can be attributed to both a lower number of charge carriers and a lower mobility. The mobility is extracted from the transfer curve of OFET devices fabricated under the same conditions as the two terminal chemiresistor, Figure S2, Supporting Information. The saturated mobility of PQT12 is several orders of magnitude lower at 9×10^{-5} cm^2 V^{-1} s^{-1} compared to 0.005 cm^2 V^{-1} s^{-1} for P3HT. Mobility contributes to the speed of charge carriers through the active channel and agrees with the lower degree of interchain packing order indicated by the lack of vibronic peaks measured in the PQT12 absorbance spectrum, Figure 1c. The charge carrier density in neat PQT12 is also lower, in part due to the deeper HOMO level of PQT12, creating a larger injection barrier at the gold electrode, Figure S3, Supporting Information.

Despite the lack of ground state doping observed in the absorbance spectra, there is a significant enhancement in drain current measured when P3HT and PQT12 are blended with SSIL. Figure 1e shows the current enhancement from neat to blend by examining the change in drain current (ΔI_D). P3HT:SSIL I_D is increased by an order of magnitude to 42 µA due to the ionic liquid induced electrochemical doping.[15] The electrical performance of PQT12 changes dramatically when blended with SSIL, increasing by four orders of magnitude to 4 µA at an applied voltage of −2 V. Although P3HT's drain current saturates at −2 V, the applied voltage dependence of PQT12 increased further achieving the highest drain current at 65 µA at −3 V. The increase in current is fully reversible and repeatable, as shown by repeated cycles of the driven voltage dependence, Figure S4, Supporting Information, confirming there is no permanent interaction with the ionic liquid. Previous studies with solid-state ionic liquids confirm that SSIL is an insulator and an SSIL only device measures no current.[13] The solid-state nature of the ionic liquid in a solid-state thin film means there is no ion mobility and electrochemical impedance spectroscopy measurements show there is no ionic contribution to the conductivity increase, Figure S5,

© 2023 The Authors. Advanced Materials published by Wiley-VCH GmbH

15214095, 2024, 20, Downloaded from https://onlinelibrary.wiley.com/doi/10.1002/adma.202211184 by Imperial College London, Wiley Online Library on [17/06/2024]. See the Terms and Conditions (https://onlinelibrary.wiley.com/terms-and-conditions) on Wiley Online Library for rules of use; OA articles are governed by the applicable Creative Commons License

Supporting Information.[36,37] This confirms SSIL as an active component in the current enhancement through reversible interactions with the polymer under an applied bias. We can therefore conclude that SSIL electrochemically dopes both P3HT and PQT12. The magnitude of current enhancement has been shown to be related to the OFF current of the neat polymer, where the maximum current achieved may be linked to the total charge carrier density concentration.

2.2. Resonant Raman Spectroscopy

Resonant Raman spectroscopy was used to investigate the molecular level vibrations and probe the polaronic peak signatures of the two conjugated polymers.[10] The Raman peak assignment is shown in detail in Figure S6, Supporting Information and summarized in Table S2, Supporting Information. The Raman signal of P3HT is formed of three main peaks, C═C, the double bonds of the thiophene rings, at 1446 cm^{-1}, the C—$C_{intra,}$ the single bond within the thiophene ring, at 1381 cm^{-1}, and C—C_{inter}, the single interunit bond between two adjoining thiophene rings, at 1210 cm^{-1}.[38] In the case of PQT12, these peaks undergo a peak splitting showing a difference between the vibrational stretch of each bond in the outer rings with side chains attached ($T_{side\text{-}chain}$) and the inner rings with no side chain (T_{bare}). This splitting between the two types of rings allows us to examine the effect of side-chain density on the conjugated backbone, thiophene rings, and even on individual bonds. When blended with SSIL, the normalized Raman spectrum of P3HT (Figure S6a, Supporting Information) shows no change in peak position or relative peak intensity, indicating no change in bond length or redistribution of π-electron density occurs with the addition of SSIL. In PQT12:SSIL (Figure S6b, Supporting Information), the peak position stays constant while the relative intensity of the C—C single bonds increases slightly; in particular, the $T_{side\text{-}chain}$ C—C_{intra} peak becomes more prominent with a greater separation from its neighboring peaks. This suggests that in the ground state, a molecular confirmational change occurs in PTQ12 when blended with SSIL, likely caused by a difference in environment between $T_{side\text{-}chain}$ and T_{bare} rings.

2.3. Electric Field Dependent Raman Spectroscopy

In order to track polaron formation and its associated polymer structure changes in a conjugated polymer:SSIL blend, in situ electric field dependent Raman spectroscopy (EFDRS) is used. The Raman peak changes of the active channel under applied drain voltage were used to probe the appearance of polaronic signals and understand the evolution of long-lived stable polarons in the film.[15] Electrochemical doping with solid-state ionic liquid increases the density of long-lived polarons, facilitating the spectral visualization of polaron formation in thin films. This has many advantages over using in situ electrochemical resonant Raman spectroscopy in an electrochemical cell as the bias conditions are more consistent with solid-state device operational conditions. Therefore, we will focus on the polaron formation in blended films; and then, link to the neat EFDRS.

Figure 2a shows the EFDRS of P3HT:SSIL; the neutral peaks remain broadly constant as the V_D is increased from 0 to −1.0 V. At −1.5 V, there is a dramatic change in peak position and intensity. The overall Raman peak intensity increases as the polarons form in the channel as they are more resonant with the excitation wavelength (785 nm) than the neutral state. With polaron formation, the C═C peak shifts to lower wavenumber (1412 cm^{-1}) indicating an increase in bond length of the double bond. The relative peak intensity of the C—C_{intra} and C—C_{inter} peaks increases with respect to the C═C peak as the π-electron density redistributes from double to single bonds under polaron formation. After −1.5 V, there is a drop in overall intensity and a slight further downshift of the C═C peak to 1407 cm^{-1}. The decrease in intensity may be indicative of bipolaron formation as the polaronic resonance with the excitation laser is reduced as the bipolaron band in the mid IR increases.[6] Beyond −1.5 V, further voltage application does not induce any more changes to the peak positions or relative intensities suggesting no further structural changes occur. The in situ current (Figure 2d) also shows an increase by six orders of magnitude going from 0 to −1.5 V. At applied voltages greater than −1.5 V, the drain current saturates, which is consistent with the unchanging Raman spectra and indicating no further structural change occurs.

Both P3HT and PQT12 show many similarities in the absorbance bands (Figure S7, Supporting Information) and Raman signatures (Figure S6, Supporting Information). Thus, PQT12 can be probed by EFDRS under the same conditions as P3HT; this allows a detailed investigation of the effect of side-chain density on polaron formation. Figure 2b shows the EFDRS for PQT12:SSIL. While the peak changes follow the same principal shifts from neutral to polaronic, the details show an incredible difference from P3HT. There is the same shift from the neutral Raman signature, with π-electron density focused on the C═C peak, to the polaronic signature, where C—C peaks increase in relative intensity. Contrary to the peak signature changes in P3HT, the C═C does not shift to lower wavenumber but stays constant at 1460 cm^{-1}. The greatest difference between the EFDRS of PQT12 and P3HT is the saturation of peak changes. While P3HT remains at constant wavenumber and intensity at applied voltages above −2 V, PQT12 peaks continue to increase in intensity even up to −10 V. The in situ current (Figure 2d) increase occurs in distinct regimes; initially the current increases linearly in line with Ohm's law; at −2 V, there is an increase in gradient with a strong current injection up to −4.5 V before slowing again and eventually saturating around −6 V. The threshold voltage for polaron formation is correlated with the onset of oxidation in CV measurements but also has contributions from the device architecture and experimental conditions. PQT12 measures a slightly higher threshold voltage in line with the deeper HOMO level and oxidation onset vs Ag, Figure S7, Supporting Information. The much higher applied voltage for saturation of current and Raman peak changes indicates a significant increase in the number of polarons generated and delocalized in PQT12 (−4.5 V) compared to P3HT (−2 V).

The degree of polaronic signature in PQT12 can be compared by tracking the change in intensity between the C—C_{intra} peak and C═C peak over the applied voltages, $I_{C-C}/I_{C=C}$ (Figure 2e).[38] In the neutral state, the C═C is by far the most intense peak, with an initial intensity ratio of 0.4, comparable to P3HT at 0.3. While

© 2023 The Authors. Advanced Materials published by Wiley-VCH GmbH

15214095, 2024, 20, Downloaded from https://onlinelibrary.wiley.com/doi/10.1002/adma.202211184 by Imperial College London, Wiley Online Library on [17/06/2024]. See the Terms and Conditions (https://onlinelibrary.wiley.com/terms-and-conditions) on Wiley Online Library for rules of use; OA articles are governed by the applicable Creative Commons License

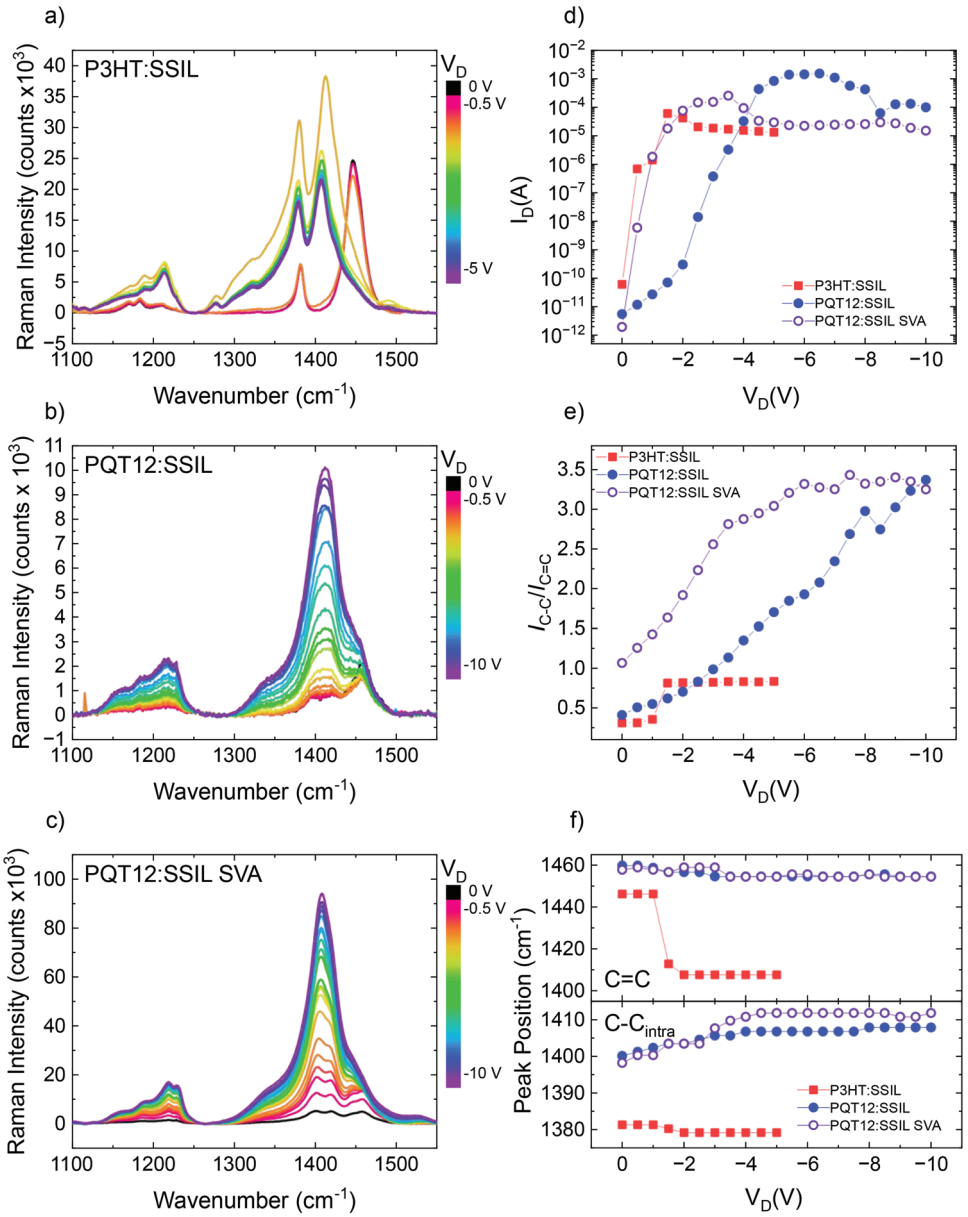


Figure 2. In situ electric field-dependent Raman spectroscopy (EFDRS) with 785 nm excitation for P3HT:SSIL (a), PQT12:SSIL (b), and PQT12:SSIL SVA (c). d) Current measured during EFDRS. e) Raman peak intensity ratio between C—C_{intra} and C=C ($I_{C-C}/I_{C=C}$). f) Peak position of the C=C peak (top) and C—C_{intra} peak (bottom) as a function of applied voltage.

P3HT increases to 0.8 and then levels off at −1.5 V, PQT12 continues to rise with the intensity of the C—C_{intra} peak increasing with voltage. At −10 V, the $I_{C-C}/I_{C=C}$ is 3.4 showing a very strong rearrangement of π-electron density to the C—C_{intra} bonds. Another contrasting signature to P3HT is the changes in peak position (Figure 2f), where P3HT shows a 40 cm^{-1} shift in C=C peak position and slight lowering of the C—C_{intra}; PQT12 shows an increase in C—C_{intra} peak position by 9 cm^{-1} while the C=C peak maintains the same position as a small shoulder to the much more intense C—C_{intra} peak. The shift in C—C_{intra} indicates a change in environment of the T_{bare} and $T_{side\text{-}chain}$ C—C_{intra} bonds to become more alike as the polaron forms, suggestive of a greater degree of delocalization along the backbone compared to the neutral. The lack of C=C peak shift implies there is less reorganization of π-electron density and lower bond length change in PQT12 compared to P3HT.

Based on the significantly different EFDRS characteristics between PQT12:SSIL and P3HT:SSIL, we can elucidate a different mechanism of polaron formation in these two solid-state chemiresistor blends. Introducing different environments of the thiophene rings through lowering the side-chain density induces changes in the way polarons form and localize along the PQT12 conjugated backbone. The larger changes in relative peak intensities show that there is more significant redistribution in π-electron density in PQT12, suggesting a higher density of polarons is present within the channel. The preservation of the

© 2023 The Authors. Advanced Materials published by Wiley-VCH GmbH

15214095, 2024, 20, Downloaded from https://onlinelibrary.wiley.com/doi/10.1002/adma.202211184 by Imperial College London, Wiley Online Library on [17/06/2024]. See the Terms and Conditions (https://onlinelibrary.wiley.com/terms-and-conditions) on Wiley Online Library for rules of use; OA articles are governed by the applicable Creative Commons License

peak position indicates there are considerably less bond length changes; and hence, less structure changes upon polaron formation in PQT12.

The EFDRS of neat P3HT and PQT12 are shown in Figure S8, Supporting Information. Due to the lower conductivity and number of charge carriers, neat polymers have a much lower polaron density, which is more difficult to visualize in EFDRS. We can examine the initial steps in polaron formation between 0 and −5 V. Neat P3HT shows no peak changes or relative peak intensity changes as the applied bias increases and the current increases only one order of magnitude as the V_D is increased from −0.5 to −5 V. This is consistent with a large structural change required to form a polaron and suggests that the high population of minority charge carriers shown in Figure 1d is responsible for the flow of charges through the film. Neat PQT12 shows the same initial increase in the C─C_{intra} peaks present in the PQT12:SSIL EFDRS; the $I_{C-C}/I_{C=C}$ increases and the current increases by three orders of magnitude. This indicates that formation of initially localized polarons with minimal structural change is a polymer property of PQT12.

2.4. Molecular Weight Impact on Polaron Formation

An important consideration is the molecular weight dependence of conjugated polymers. The effect of molecular weight (M_w) on P3HT electrical and morphological characteristics has been extensively studied.[39–45] In particular, the microstructure is highly dependent on M_w. At low M_w, the short chains tend to form poorly connected chain extended crystals.[3] Beyond a critical M_w (34 kgmol^{-1}),[42] the longer chains entangle in solution resulting in a thin film microstructure containing crystalline domains interconnected by tie chains through amorphous regions.[46] The effect of M_w on the conjugated polymer:SSIL blend has previously been shown to be consistent with the chain packing behavior of the neat polymer.[15] As the electrochemical doping by SSIL is only able to enhance the charge carrier characteristics of the polymer, a well interconnected network of polymer chains and sufficient percolation of the ionic liquid into the polymer chain packing structure is required for efficient charge transport and polymer-SSIL interaction. Figures S1 and S9, Supporting Information show that low M_w P3HT:SSIL blends result in isolated domains of P3HT surrounded by a matrix of SSIL, resulting in limited interaction between the two components and poor enhancement of electrical characteristics.

Despite the lower M_w of PQT12 (14 kg mol^{-1}), the PQT12:SSIL blend shows a comparable topography to that of high M_w P3HT:SSIL, where a high surface roughness and large domain pattern indicate blending and intercalation of the ionic liquid into the polymer chain packing, unlike the segregation of low M_w P3HT:SSIL.This difference in blending morphology is also apparent in the electrical characterization of the PQT12:SSIL blend, where the electrochemical doping and current enhancement of PQT12 by SSIL does not follow the trend set by P3HT:SSIL of equivalent M_w. Figure S1, Supporting Information, shows the largest current values are achieved with PQT12:SSIL (65 µA) with an increase of several orders of magnitude over neat PQT12, indicating a strong electrochemical doping interaction with SSIL. For comparable M_w of P3HT, the current enhancement after blending with SSIL is minimal due to the poor intermixing. At 10 kg mol^{-1}, the driven voltage dependence decreases from neat to the SSIL blend and at P3HT 20 kg mol^{-1}, there is a small increase in current, reaching a maximum of 2 µA. Thus, the intermixed morphology of PQT12:SSIL results in strong signatures for electrochemical doping and enhanced current levels relative to the neat films, akin to the high M_w P3HT:SSIL. As the high M_w P3HT and low M_w PQT12 blends exhibit the strongest electrochemical doping effects, they are best suited for the detailed analysis of polaron formation detailed below.

To examine the M_w dependence on polaron formation, EFDRS was measured over a variety of M_w of P3HT between 0 and -2 V. Figure S10, Supporting Information, compares the EFDRS of the high performing P3HT used in this study (58 kgmol^{-1}) to a range of molecular weights. Above the critical M_w (34 kg mol^{-1}),[42] EFDRS shows a single step jump from neutral to polaronic Raman signature, indicating a shift from benzoidal to quinoidal within a 0.1 V region. Below the critical M_w, the change from neutral to polaronic Raman signature is slower. At −1 V, the polaronic C═C peak at 1412 cm^{-1} starts to appear as a shoulder of the neutral peak and gradually increases in intensity until it becomes the highest intensity peak and relative peak changes saturate before −2 V. This can be attributed to the presence of unconnected chain extended crystallites in low M_w P3HT; each isolated domain will have a slightly different threshold for polaron formation and the Raman signal contains a mix of domains where polarons have formed and structural change has occurred as well as domains that remain neutral.

In summary, the Raman signature changes indicative of polaron formation in P3HT are consistent across a wide range of M_w and microstructures. The degree of polaron formation, measured by the $I_{C-C}/I_{C=C}$ ratio (Figure S10f, Supporting Information) saturates at 0.8–0.9 for all P3HT M_w showing that the total redistribution of π-electron density is consistent across significantly different chain packing and charge-transport behaviors. In addition, the shift of the C═C (Figure S10g, Supporting Information) from neutral to polaronic is consistently between 30 and 40 cm^{-1}, indicating the required lattice distortion to accommodate the polaron is uniform regardless of molecular weight. Such distinctive polaron-induced structural changes that are independent of P3HT M_w confirm that the lack of C═C structural changes observed in PTQ12 are not due to different M_w but due to the different side-chain density. The polaronic Raman signatures of PQT12 are notably different to P3HT. The C═C peak does not shift, indicating a reduced structural change; and therefore, lower lattice distortion upon polaron formation. The $I_{C-C}/I_{C=C}$ increases dramatically to seven times the neutral ratio, indicating a much higher density of polarons can be generated in PQT12. These observations confirm that the polaron formation is primarily dependent on the intrinsic molecular structure of the polymer, not M_w.

2.5. Morphological Impact on Polaron Formation

To further study the effect of morphology on the conjugated polymer backbone, solvent vapor annealing (SVA) was performed on the chemiresistor films. SVA can increase the degree of chain packing; and therefore, charge-transport properties of solution

© 2023 The Authors. Advanced Materials published by Wiley-VCH GmbH

15214095, 2024, 20, Downloaded from https://onlinelibrary.wiley.com/doi/10.1002/adma.202211184 by Imperial College London, Wiley Online Library on [17/06/2024]. See the Terms and Conditions (https://onlinelibrary.wiley.com/terms-and-conditions) on Wiley Online Library for rules of use; OA articles are governed by the applicable Creative Commons License

processed polymer films.[47] PQT12 has been shown to be a highly orderable material under a variety of pre and post processing techniques including SVA.[48–51] In particular, SVA has been shown to change the packing conformation and side-chain alignment, creating a more uniform film with improved mobility.[50] This can be useful as a low temperature annealing process due to the low transition point of SSIL.[52] In this study, mild SVA (40 °C with $CHCl_3$) was used to enhance the thin film packing without damaging the semicrystalline properties of SSIL. In this study, we aimed to utilize the enhancement in packing conformation of PQT12 via SVA to understand the differences observed between $T_{\text{side-chain}}$ and T_{bare} in polaron formation.

The effects of SVA were first characterized to confirm that the electrical properties and electrochemical doping were not damaged by prolonged exposure to solvent and to quantify the changes in molecular order. The absorbance spectra (Figure S12a, Supporting Information) for both P3HT and P3HT:SSIL showed a relative increase in the 600 nm shoulder, indicating an increase in aggregation.[53] In addition, there is a decrease in the vibronic 0–1 peak at 525 nm with respect to the 0–0 peak at 540 nm, resulting in an increase in the ratio of (A_{0-0}/A_{0-1}), indicating increased ordering within the aggregates.[54] Microscopy imaging (Figure S13b, Supporting Information) shows the formation of fibrous clusters in the P3HT:SSIL film; however, there is little change in morphology for the surrounding regions with respect to the as cast film, confirmed by AFM (Figure S9c, Supporting Information). These clusters are likely the root of the increased ordering observed in the absorbance as P3HT is known to undergo segregation and fibril formation under SVA.[55,56] The segregation visualized in the microscopy images correlates with the reduced I_D measured in the driven voltage dependence, Figure S12b, Supporting Information. While there are areas of greater chain ordering, the interconnected network of polymer chains is disturbed, which limits its charge transport through the film. Consequently, the EFDRS of P3HT:SSIL SVA shows no difference from the as cast (Figure S12c,d, Supporting Information), indicative of no changes in the nature of polaron formation and delocalization after SVA.

Interestingly, there is a significant change to the film morphology when PQT12:SSIL undergoes SVA. Optical microscopy images (Figure S13c,d, Supporting Information) show a smaller but consistent change across the whole film, with the blue regions transitioning from small angular domains to larger more rounded domains. Correlation with AFM imaging confirms the presence of the large flat domains above the mean film height, Figure S9f, Supporting Information. We propose that these features are unmixed SSIL domains that have grown under SVA.[15] However, absorbance spectra of PQT12 and PQT12:SSIL showed no relative peak changes, Figure S12a, Supporting Information, suggesting there is no change to the polymer chain ordering after SVA. This suggests that while there are significant macroscopic changes to the film morphology, polymer conformation and packing is unaffected. The most significant change after SVA is in the driven voltage dependence; PQT12:SSIL SVA increases by an order of magnitude above as cast to 155 µA, (Figure S12b, Supporting Information). This further enhancement of current indicates that the strength of electrochemical doping has increased, suggesting that the nanoscale changes in the film have strengthened the interaction between SSIL and the conjugated polymer. This indicates there is no change in conformational order for PQT12 polymer chains but the interaction with the ionic liquid increases. It is likely that the SVA allows the SSIL to redissolve and better permeate the polymer chain packing, allowing for a stronger ionic liquid:polymer backbone interaction.

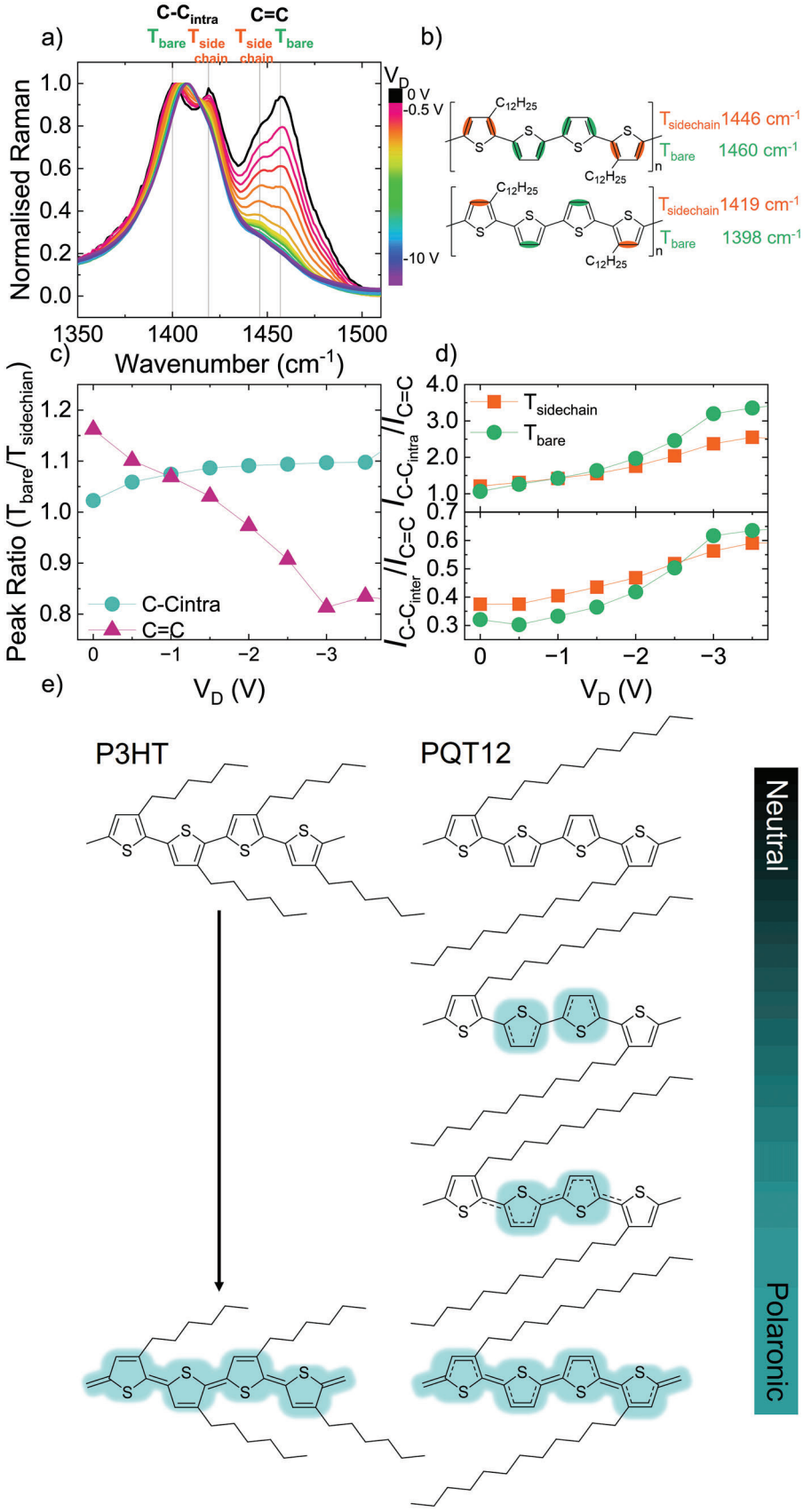
The aim of SVA is to enhance the chain packing behavior of PQT12, enhancing the distinction between thiophene ring environments under more crystalline conditions; and therefore, better visualize the changes between $T_{\text{side-chain}}$ and T_{bare} under polaron formation. Despite the lack of changes to absorption, the steady state Raman is more sensitive to small changes in molecular conformation[57] and confirms SVA has brought about environmental changes to the $T_{\text{side-chain}}$ and T_{bare} peaks. After the SVA of PQT12:SSIL, (Figure S6c, Supporting Information), the relative peak intensity of the C—C_{intra} peaks increase compared to the as cast device and the separation between the two peaks is more prominent. Interestingly, there is also the appearance of a shoulder peak on the C═C vibration at 1446 cm^{-1}; this additional shoulder is not present in the as cast PQT12:SSIL but aligns with the C═C vibration of P3HT. The increased ordering has created a greater distinction and peak splitting of the double bonds between substituted and unsubstituted thiophene rings in addition to the single carbon—carbon bonds seen in as cast films. This can be seen in previous studies where the different processing methods used to improve polymer chain alignment of PQT12 films have enhanced the shoulder at 1446 cm^{-1}.[51,58]

The EFDRS of PQT12:SSIL SVA can be seen in Figure 2c. The overall peak changes are consistent with the changes seen with as cast PQT12:SSIL; however, they occur at a lower applied voltage confirming it is easier to form polarons as the polymer is more ordered. The first regime of polaron formation occurs between 0 and −3 V, where there is a rapid increase in current accompanied by an increase in peak ratio and shift in peak position, after which all three of these parameters saturate and remain relatively constant with voltage. We can follow the process of polaron formation in the nonuniform backbone of PQT12 using detailed analysis of the spectral changes of the two ring types. Due to the increased order and better separation of Raman peaks between $T_{\text{side-chain}}$ and T_{bare}, the EFDRS of PQT12:SSIL SVA allows a clearer picture of the changes to vibrational environments as the different rings undergo polaron formation. **Figure 3**a shows the EFDRS of PQT12:SSIL SVA normalized to the maximum intensity peak, the C—C_{intra} of T_{bare} at 1398 cm^{-1}. Here, the relative peak intensity of the four in-plane ring skeleton modes (Figure 3b) can be tracked as they change with voltage.

As polarons form in the polymer, the peak intensity ratio of each mode is tracked for the thiophenes without side chains (T_{bare}) to the thiophenes with side chains ($T_{\text{side-chain}}$), shown in Figure 3c. This allows comparison of rates of change for the two different environments of C═C and C—C. At 0 V, the Raman peak intensity of the T_{bare} C═C peak was higher than that of $T_{\text{side-chain}}$, suggesting a greater distribution of π-electron density was localized to the double bonds of the bare rings in the ground state. As the applied voltage was increased, there was a rapid decrease in peak intensity ratio from 1.2 at 0 V to 0.8 at 3 V. This indicates the redistribution of electron density upon polaron formation starts with the T_{bare} C═C bonds loosing double bond character. The C—C_{intra} intensity ratio gradually increases as the electron density redistributes to the T_{bare} C—C_{intra} at a

© 2023 The Authors. Advanced Materials published by Wiley-VCH GmbH

15214095, 2024, 20, Downloaded from https://onlinelibrary.wiley.com/doi/10.1002/adma.202211184 by Imperial College London, Wiley Online Library on [17/06/2024]. See the Terms and Conditions (https://onlinelibrary.wiley.com/terms-and-conditions) on Wiley Online Library for rules of use; OA articles are governed by the applicable Creative Commons License



© 2023 The Authors. Advanced Materials published by Wiley-VCH GmbH

15214095, 2024, 20, Downloaded from https://onlinelibrary.wiley.com/doi/10.1002/adma.202211184 by Imperial College London, Wiley Online Library on [17/06/2024]. See the Terms and Conditions (https://onlinelibrary.wiley.com/terms-and-conditions) on Wiley Online Library for rules of use; OA articles are governed by the applicable Creative Commons License

15214095, 2024, 20, Downloaded from https://onlinelibrary.wiley.com/doi/10.1002/adma.202211184 by Imperial College London, Wiley Online Library on [17/06/2024]. See the Terms and Conditions (https://onlinelibrary.wiley.com/terms-and-conditions) on Wiley Online Library for rules of use; OA articles are governed by the applicable Creative Commons License

greater rate than to the $T_{\text{side-chain}}$ C—C_{intra}. The peak ratio can be further examined by looking at the relative intensity of the single to double bonds in more detail, differentiating between ring type instead of simply the maximum intensity (Figure 3d). In addition to the ratio of the intra C—C bonds to C═C, we will also examine the interunit bonds creating two different ratios $I_{\text{C–Cintra}}/I_{\text{C=C}}$ and $I_{\text{C–Cinter}}/I_{\text{C=C}}$. The $I_{\text{C–Cintra}}/I_{\text{C=C}}$ starts off lower for T_{bare} than $T_{\text{side-chain}}$ at 0 V and then increases from 1.1 to 3.2 by $V_{\text{D}} = -3$ V while $T_{\text{side-chain}}$ only reaches 2.4. This indicates that the charge redistribution and polaron formation occur faster on the unsubstituted thiophenes. Similarly, by the same applied voltage, $I_{\text{C–Cinter}}/I_{\text{C=C}}$ was higher for T_{bare} than $T_{\text{side-chain}}$, allowing for more π-electron delocalization on the interunit bond between the two inner thiophene rings than the interunit bonds flanking the thiophenes with side chains. These results demonstrate the role of side chains on the polaron formation, where the polaron formation on unsubstituted thiophenes occurs first with less structural change and greater π-electron redistribution.

2.6. Proposed Polaron Formation

We use the experimental polaronic progression from EFDRS to propose a model of polaron formation, Figure 3e. The electrochemical doping of the conjugated polymer by the solid-state ionic liquid allows us to examine the stages of polaron formation through changes to the vibrational modes of the polymers. For P3HT, there is a simultaneous shift in C═C and change in $I_{\text{C–C}}/I_{\text{C=C}}$ ratio, suggesting that P3HT requires large geometry change and lattice distortion to allow polaron formation and π-electron delocalization in one step. The PQT12 spectra, on the other hand, undergoes a progression of structural changes toward polaronic signatures; hence, indicating that polaron formation and delocalization along the backbone occur over a series of stages. A simplified schematic diagram of the proposed polaron formation process is shown in Figure 3e and outlined below.

Step 1 is the initial localization of charge on T_{bare} rings. From the EFDRS in Figure 3c, the C═C bond of the T_{bare} rings is the first to lose π-electron density and show a drop in Raman peak intensity; this is closely followed by the gain in intensity of intra C—C bond on the same ring. This suggests that localized polaron formation first occurs on the T_{bare} rings where no side chains are attached to thiophene rings. Further support comes from the peak intensity ratios where the $I_{\text{C–Cintra}}/I_{\text{C=C}}$ of T_{bare} increases faster than that of $T_{\text{side-chain}}$ showing the redistribution of π-electron density within the ring is faster and easier on the inner thiophenes, further indicating that polarons initially form with more localization to unsubstituted thiophene rings.

Step 2 is the delocalization to the interunit bond between the two T_{bare} rings. This is indicated by the delayed increase in T_{bare} $I_{\text{C–Cinter}}/I_{\text{C=C}}$ compared to T_{bare} $I_{\text{C–Cintra}}/\text{I}_{\text{C=C}}$. While the intra peak ratio started to increase almost immediately after voltage was applied, the ratio for the interunit bond initially remained steady until −1 V (Figure 3d); suggesting that polarons initially form inside the T_{bare} rings as more localized polarons and only once the π-electron density on the T_{bare} ring has built up does delocalization along the backbone occur. Then comparing $I_{\text{C–Cinter}}/I_{\text{C=C}}$ of T_{bare} to that of $T_{\text{side-chain}}$ shows that the next step of delocalization is preferentially to the interunit C—C_{inter} bond between the T_{bare} rings. This is likely due to the lower barrier of steric hinderance between the two bare rings than those with side chains.

Step 3 is the delocalization to outer $T_{\text{side-chain}}$ rings. Figure 3d shows that both $I_{\text{C–Cintra}}/I_{\text{C=C}}$ and $I_{\text{C–Cinter}}/I_{\text{C=C}}$ of $T_{\text{side-chain}}$ increases at greater applied voltage than those of T_{bare}. This indicates that the process of π-electron distribution from double to single bond in the $T_{\text{side-chain}}$ rings occurs after that of T_{bare}. In addition, the $T_{\text{side-chain}}$ ratios saturate at a lower value than T_{bare} also implying that the degree of polarization is less for the rings with side chains. Unlike in P3HT, PQT12 retains some of the C═C character even under the fully delocalized polaron as the bond length change is smaller and the vibrational C═C peak does not change in wavenumber.

Above V_{D} of −3 V, there is no further increase in current; Figure 2d and the change in relative peak intensities levels off, Figure 3d. This indicates that the major geometry changes have occurred and no further polarons are formed. Understanding of the multistep polaron formation process also offers insight into the electrochemical doping mechanism of SSIL. The solid-state ionic liquid intercalates more easily into the conjugated units in the backbone when no side chains exist, preferentially interacting with the T_{bare} rings on PQT12 polymer backbone. This is likely due to a combination of the lower steric hinderance and the lower energetic barrier to polaron formation for the rings with no side chains.

2.7. Simulated Lattice Rearrangement

To understand the Raman spectral changes in EFDRS and confirm the model for polaron formation, we used density functional theory (DFT) to simulate the geometry changes upon polaron formation. DFT simulations are carried out on a single isolated polymer chain in the gas state with optimized geometries at the minima of the potential energy surface. There are significant differences between optimized simulated molecules and the real experimental conditions. DFT calculations are particularly beneficial in correlation with Raman spectroscopic analysis as Raman measures changes to the intrachain π-electrons.[59] Here, we use comparison between simulated P3HT and simulated PQT12 oligomers to decouple the intramolecular structure induced effects from interchain properties of solid-state thin films.

Reorganization energy (*RE*) is the energy required for lattice distortion upon polaron formation.[60] The inner *RE* corresponds to the sum of the geometry relaxation energies required for the structural relaxation of the molecule to accommodate the injected charge.[61,62] The outer RE is typically several orders of magnitude

Figure 3. a) Normalized EFDRS for PQT12:SSIL SVA. b) Raman peak assignment showing a peak splitting between thiophene rings with ($T_{\text{side-chain}}$) and without (T_{bare}) side chains attached. c) Peak splitting ratio ($T_{\text{bare}}/T_{\text{side-chain}}$) for the C═C and C—$C_{\text{intra}}$ peaks. d) Raman peak intensity ratio between C—C and C═C ($I_{\text{C–C}}/I_{\text{C=C}}$) for C—$C_{\text{intra}}$ (top) and C—C_{inter} (bottom) split for $T_{\text{side-chain}}$ and T_{bare} as a function of applied voltage. e) Schematic diagram of the charge distribution and bond rearrangement during polaron formation.

© 2023 The Authors. Advanced Materials published by Wiley-VCH GmbH

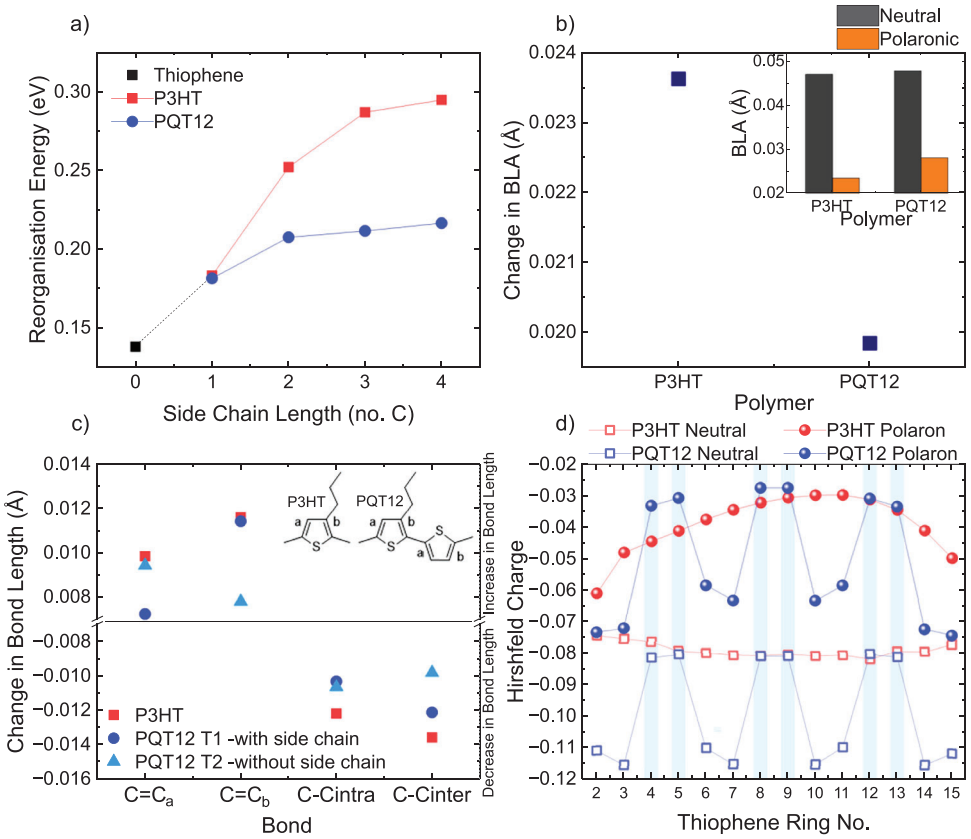


Figure 4. DFT Simulations. a) Reorganization energy as a function of side-chain length for P3HT and PQT12 oligomer of 16 thiophenes in length. Change in geometric properties from neutral to polaronic (+1) for oligomer of 16 thiophenes long with propyl side chains. b) Change in bond length alternation (BLA) with insert as BLA. c) Change in bond length. d) Hirshfeld charges of each ring in simulated backbone with PQT12 side-chain positions marked by shaded areas.

lower than the inner component and is derived from rearrangement of the surrounding medium;[63,64] this will not be discussed here in the comparison of initial polaron formation on a single polymer chain.[60] **Figure 4**a shows the simulated inner RE calculated for a series of side-chain lengths. RE initially increases with an increase in side-chain length showing the importance of computational accuracy in simulations. For longer side-chain lengths, RE levels off, maintaining a 0.08 eV energy gap between P3HT and PQT12. The lower RE confirms the energy required for structural change to form a polaron is lower and therefore more favorable in PQT12, consistent with the smaller structural changes observed experimentally. To understand how the difference in structural factors contribute to the lower RE, further DFT analysis was carried out to simulate the lattice distortion under polaron formation.[64]

To support the RE calculations, bond length alternation (BLA) was calculated. The BLA is the average difference between the length of the C—C and C═C[65,66] and the change to BLA (ΔBLA) upon adding a charge can be used to assess the lattice distortion upon polaron formation, (Figure 4b). The ΔBLA is higher for P3HT (0.024) compared to PQT12 (0.020), which confirms that a larger structural change is required in P3HT upon polaron formation, which correlates with its higher RE. Table S3, Supporting Information, shows that P3HT starts with an initially twisted backbone in comparison to PQT12, which will contribute to the RE required to planarize upon polaron formation.

DFT simulation of the neutral and polaronic states gives the final optimized geometry for the oligomer in the gas state. This allows detailed comparison of the observed experimental changes with the changes to individual bonds from the neutral state to their final state under a stable fully delocalized charge. We can look at the mean bond length change to each bond type to understand the effect of side-chain density on lattice distortion (Figure 4c). In both P3HT and PQT12 $T_{\text{side-chain}}$, the C═C$_{b,}$ with side chain attached, increases by a greater magnitude than C═C$_{a,}$ on the opposite side of the same ring with no side chain. This indicates that the side chain induces a greater lattice distortion to accommodate the polaron. In PQT12 T_{bare}, both C═C bonds have no side chain attached and the overall change in bond length is lower than in P3HT. Similarly, the single bond lengths also indicate that rings without side chains undergo less structural change. Specifically, for T_{bare}, the C—C$_{\text{inter}}$ bond length change is significantly lower, indicating that less lattice reorganization is required to stabilize the charge between the inner rings. The simulated geometry changes confirm that to stabilize a charge in PQT12, significantly less structural change is required across all geometry metrics. This correlates with the lower magnitude Raman peak shifts measured experimentally for PQT12, confirming

© 2023 The Authors. Advanced Materials published by Wiley-VCH GmbH

15214095, 2024, 20, Downloaded from https://onlinelibrary.wiley.com/doi/10.1002/adma.202211184 by Imperial College London, Wiley Online Library on [17/06/2024]. See the Terms and Conditions (https://onlinelibrary.wiley.com/terms-and-conditions) on Wiley Online Library for rules of use; OA articles are governed by the applicable Creative Commons License

15214095, 2024, 20, Downloaded from https://onlinelibrary.wiley.com/doi/10.1002/adma.202211184 by Imperial College London, Wiley Online Library on [17/06/2024]. See the Terms and Conditions (https://onlinelibrary.wiley.com/terms-and-conditions) on Wiley Online Library for rules of use; OA articles are governed by the applicable Creative Commons License

that a lower degree of structural change occurs upon polaron formation.

The charge of each thiophene ring along the chain was calculated by summing the atomic charge of each atom in the ring calculated by Hirshfeld population analysis (Figure 4d).[67,68] Neutral and polaronic P3HT show uniform charge distribution across the backbone, which suggests full polaron delocalization across the oligomer length. In contrast, neutral PQT12 has uneven charge distribution on the T_{bare} rings with a higher magnitude of Hirschfeld charge. The charge distribution profile is maintained upon the addition of positive charge; therefore, the polaron is also non-uniformly delocalized. The higher magnitude Hirshfeld charge supports the proposal that the partial charges tend to reside on the T_{bare} rings and remain there even after polaron delocalization.[69]

Overall, DFT simulation has been used to confirm that charging P3HT results in greater structural reorganization, with larger RE and changes in geometry upon polaron formation compared to PQT12. This correlates well with the single step polaron formation seen in EFDRS, with a critical input voltage being required to give sufficient energy to initiate polaron formation and lattice distortion. In contrast, the geometry changes in PQT12 are smaller and require less energy. Comparing $T_{side\text{-}chain}$ and T_{bare} of PQT12 shows that a lower structural change is required for the thiophene rings without side chains indicating that polarons form on T_{bare} first and then delocalize along the backbone. This creates the unique mechanism of polaron formation measured in EFDRS where the stages of polaron delocalization can be observed.

2.8. Polaron Formation Influence on Electrical Properties

An in-depth understanding of the polaron formation mechanism allows a better interpretation of the origins of electrical properties. Improving both charge injection and charge transport is vital to increase the performance of organic electronic devices. There has been great success in increasing interchain charge transport in organic semiconductors, with record mobilities for conjugated polymers >10 $cm^2\ V^{-1}\ s^{-1}$.[70] This is due to detailed investigations into polymer chain packing, thin film microstructure, and charge hopping behavior.[7] Charge-injection behavior of conjugated polymers can be improved with a better understanding of polaron formation and delocalization along the backbone. This is crucial as charge injection is significantly more challenging in organic semiconductors as the contact resistance (R_c) is typically much higher than in inorganic metal–oxide–semiconductor field-effect transistors (MOSFETs).[71] While there are many device architecture methods to reduce R_C and increase the charge injection from modified electrodes,[72] it is equally important to understand the charge formation mechanism of the polymer structure as efficient delocalization and bandgap tuning can be achieved by careful molecular design.[73]

Conjugated polymers are promising candidates for use as organic thermoelectric materials. However, the current limitations of conjugated polymers stem from the lack of understanding of the structure property relationship.[74,75] Detailed understanding of polaron formation and delocalization can help to elucidate the polymer structure units that contribute to increased electrical conductivity. In addition, the increased conductivity and hole polaron density of electrochemically doped PQT12:SSIL may be of particular benefit to thermoelectric energy conversion devices as there is minimal effect on the doping levels in comparison to chemically doped polymers.[75,76] Increasing the conductivity without reducing the Seebeck coefficient (S) is essential for increasing the power factor ($PF = \sigma S^2$).[77]

As an example, we now turn to demonstrating how these different polaron formation mechanisms and associated polymer structural changes affect VOC gas sensors. Chemiresistor sensors are a conductometric device where small fluctuations in the conductivity are used to create a simple, easy to read signal of the presence of the analyte.[78] A higher conductivity of the sensing material is desired for the realization of low-cost portable sensors[79] as the greater signal to noise ratio, the greater the sensitivity and lower the detection limit.[80] The SSIL blend has been shown to form highly sensitive and selective organic gas sensors with the ability to distinguish between polar and non-polar organic solvents.[14,15] Here, we demonstrate gas sensing at an applied bias of −4 V and use the Raman probe to understand how the side-chain density and nature of polaron formation affect the sensing capabilities of the ionic liquid blend.

Figure 5 shows the gas sensing performance and in situ Raman probe of the P3HT:SSIL and PQT12:SSIL blends. The change in resistance over the baseline resistance ($\Delta R/R_0$) gives a value for percentage change, which can be used to compare devices with different absolute current measurements, Figure S14, Supporting Information. When P3HT:SSIL is exposed to acetone, there is a decrease in conductivity and an increase in the polaronic Raman intensity. As polaronic Raman signal is a good approximation of the number of polarons; this suggests that there is a greater density of polarons present in the channel.[10] However, the reduction in conductivity indicates charge transport has decreased; it is likely that the interaction between the strong dipole of polar solvent and the polar SSIL increases charge trapping and prevents the flow of holes through the film. Under toluene exposure, P3HT:SSIL measures an increase in conductivity with a much faster recovery. The polaronic Raman signal decreases in full width half maximum (FWHM), indicative of a greater ordering and planarity of the polymer.[38] This suggests that as toluene adsorbs, the electrochemical doping interaction between SSIL and polymer backbone increases, which in turn increases the polaron delocalization and planarity of the polymer chains. Given the P3HT:SSIL blend morphology, Figure S9, Supporting Information, where an ordered polymer network is surrounded by a porous, amorphous ionic liquid rich matrix, it is likely that the non-polar solvent molecules absorb in to the porous domains.[15] This causes a swelling of the SSIL domains, pushing the SSIL closer to the polymer backbone, increasing the strength of the electrochemical doping interaction and increasing the conductivity. An increase in polymer ordering is observed, by the reduction of the FWHM, as the stronger interaction leads to more uniform delocalized polarons which have a planarizing effect on the polymer backbone.

The PQT12:SSIL blend has the same thiophene-based backbone; so, it could be expected to react to VOC exposure under the same mechanism as P3HT. However, the sensing response shows that there is no selectivity between polar and non-polar solvents; Figure 5c. PQT12:SSIL reacts to acetone and toluene by

© 2023 The Authors. Advanced Materials published by Wiley-VCH GmbH

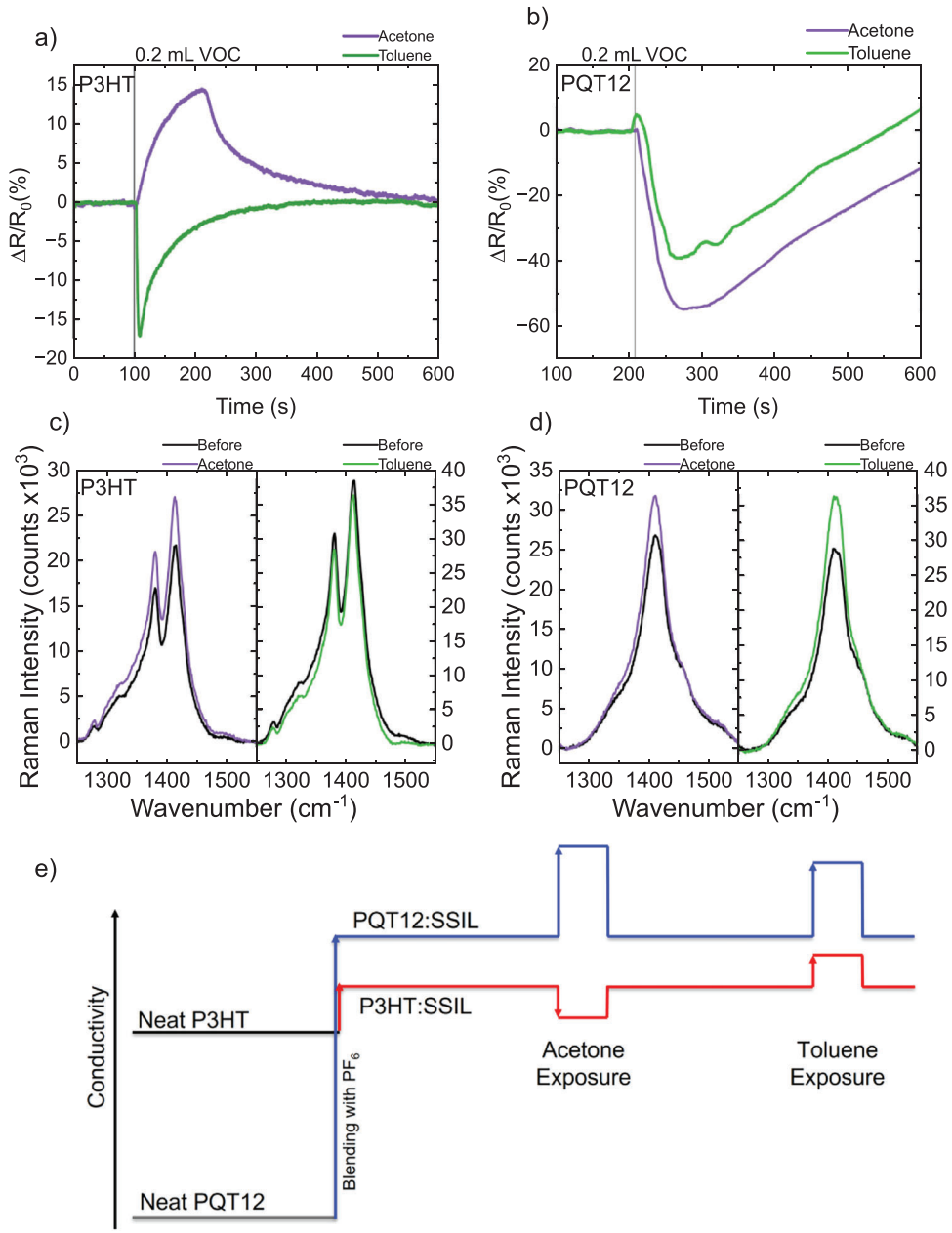


Figure 5. a,b) Percentage change in electronic resistance under acetone and toluene exposure for P3HT:SSIL (a) and PQT12:SSIL (b) under an applied $V_D = -4$ V. c,d) In situ Raman spectroscopy under VOC gas exposure for P3HT:SSIL (c) and PQT12:SSIL (d). e) Schematic diagram showing the changes in conductivity with gas exposure.

the same mechanism, the conductivity increases, and the polaronic Raman intensity increases. This suggests the number of polarons present increases whilst charge-transport levels are maintained or increased, unlike P3HT. The closer interchain packing of PQT12 has been well reported in literature;[21,81–83] this could suggest that the denser packing structure both strengthens the interaction with SSIL, which has been intercalated in solution, and prevents electrostatic interactions with solvent molecules under gas exposure. The AFM of the conjugated polymer:SSIL blends (Figure S9, Supporting Information) shows the formation of a 3D porous network structure where there are areas of closely packed polymer chains surrounded by amorphous areas of predominantly ionic liquid. It is believed that the physical adsorption of solvents will be largely into the amorphous regions. Support for this proposed mechanism comes from the higher magnitude of response to acetone exposure; as acetone is a polar solvent, the hydrophobic alkyl side chains will retract further from the polar stimuli,[84] causing a greater entrapping of the SSIL within the polymer domains with a greater increase in electrochemical doping strength.

The difference in polaron formation mechanism can explain the non-selectivity of PQT12. As polaron formation occurs in

© 2023 The Authors. Advanced Materials published by Wiley-VCH GmbH

15214095, 2024, 20, Downloaded from https://onlinelibrary.wiley.com/doi/10.1002/adma.202211184 by Imperial College London, Wiley Online Library on [17/06/2024]. See the Terms and Conditions (https://onlinelibrary.wiley.com/terms-and-conditions) on Wiley Online Library for rules of use; OA articles are governed by the applicable Creative Commons License

steps, starting with the localized polaron formation of the inner T_{bare} rings, it is expected that the main interaction of the SSIL PF_6^- anions will be with the T_{bare} rings. The interaction between the T_{bare} rings and SSIL has been shown to be stronger due to the greater degree of polarization (Figure 3d), lower reorganization energy (Figure 4a), and reduced steric hinderance of T_{bare} (Table S3, Supporting Information). When under a solvent atmosphere, the strength of interaction between T_{bare} and SSIL and steric hinderance of the longer alkyl side chains will likely prevent any chemical interaction between SSIL and the solvent molecules as it will be less energetically favorable even for highly polar solvents.

3. Conclusion

We have compared the mechanisms of polaron formation in P3HT (100% side chain) and PQT12 (50% side chain). This study focused on two devices that achieve similar current levels to make a fair comparison of the mechanism of polaron formation. The reduction in side-chain density has a significant effect on the EFDRS signatures as the PQT12:SSIL blend system is probed under applied voltage. P3HT shows a one-step polaron formation and delocalization process where there are large peak signature changes as the whole polymer chain becomes polaronic together with a large degree of structural change. In contrast, PQT12 shows a multistep process to becoming fully charged and delocalized, with a strong π-electron distribution to the C—C but without the change to C═C length signified by the change in peak position. Simulations suggest this is likely due to the inhomogeneity of the PQT12 backbone; the unsubstituted T_{bare} thiophene rings are able to induce an initially more localized polaron with less delocalization along the backbone. The lower reorganization energy and smaller simulated geometry changes point to polaron formation being easier in PQT12 due to the lower degree of structural change required. The polaron formation process starts on the inner T_{bare} rings but the lack of driving force to create a lower energy delocalized polaron could mean that it takes greater applied voltages to produce the same level of delocalized charge as in P3HT.

We have demonstrated that blending PQT12 with SSIL results in strong electrochemical doping and greater current enhancement than when blended with P3HT. Therefore, it is suggested that the PQT12:SSIL blend would be an improved chemiresistor device where high conductivities are required. However, we have shown that high electrical performance is not the critical factor for some device applications such as VOC gas sensors where the sensor selectivity is more important. While PQT12:SSIL measured a stronger sensing response, the selectivity between polar and non-polar solvents was only seen in P3HT:SSIL. This shows the polaron formation and the electrochemical doping mechanism determines the sensing mechanism and selectivity. This work importantly elucidates the polaron formation mechanisms and how it changes device operational properties is essential for designing future high-performance optoelectronic devices.

4. Experimental Section

Materials: Poly(3-hexylthiophene-2,5-diyl) (P3HT) was purchased from 1 M at a $M_w = 58$ kg mol^{-1}, $M_n = 28$ kg mol^{-1}, regioregularity 96%, and polydispersity 2.1. Full details of all P3HT samples used in M_w study can be found in Table S1, Supporting Information. Poly(3,3‴-didodecyl quaterthiophene) (PQT12) was purchased from Solarmer and measured by GPC, $M_w = 14$ kg mol^{-1} $M_n = 7$ kg mol^{-1} and polydispersity 2.0. Solid-state ionic liquid 1-dodecane-3-methylimidazolium hexafluorophosphate ($[C_1C_{12}IM^+][PF_6^-]$), was synthesized through a conventional method described elsewhere.

Film Preparation: P3HT and PQT12 blends with SSIL were dissolved in chloroform at a 5 mg mL^{-1} and stirred at 40 °C. The solutions were filtered at 0.45 µm and left for 24 h before being spin coated on to cleaned substrates at 2000 rpm 40 s^{-1}. A film thickness of 40 nm and 100 nm was deposited for the neat and blend respectively. Chemiresistor and OFET devices were fabricated using Fraunhofer silicon wafers with a silicon dioxide layer and the source and drain electrodes ($W = 2$ mm $L = 5$ µm) formed of a 10 nm ITO adhesion layer and topped with 30 nm of gold. Deposited films were dried in a desiccator overnight and stored in N_2. Film thicknesses were measured on a Bruker DektakXT at ≈40 nm for neat films and ≈100 nm for SSIL blended films. Thin films on quartz for optical measurements where prepared in the same way.

Solvent Vapor Anneal: For solvent vapor anneal P3HT and PQT12 neat and blended films were prepared from the same solution as the as cast films. Immediately after spin coating, films where sealed in a chloroform vapor at 40 °C overnight before being placed in a desiccator to remove any residual solvent. SVA films were then stored in N_2 before and between measurements.

Absorbance: The absorption of thin films on quartz was measured on Shimadzu UV-2600 UV/visible spectrophotometer with integrating sphere attachment. Air was used as a baseline reference and the thin film samples were corrected to the transmission of a clean blank quartz substrate.

Electrical Characterization: Chemiresistor performance was measured using driven voltage dependence measurement on a probe station in a nitrogen glovebox. A drain voltage was held between the source and drain electrode for 10 s and the drain current measured. The mean current for each applied voltage was extracted to evaluate the device performance. OFET transfer curves were measured on the same probe station, $V_D = -10$ V and −60 V and V_G sweep = +20 V to −60 V.

Electrochemical Impedance Spectroscopy: Electrochemical impedance spectroscopy measurements were performed using a ModuLab XM system (Solartron Analytical) at different applied DC potentials (0 and −2 V between the source and drain electrodes) applying an AC amplitude of 10 mV in the frequency range of 100 kHz to 1 Hz. The complex impedance data was fitted applying an $R_s(R_b||C)$ equivalent circuit, where R_s is the resistance of the external circuit, R_b the bulk resistance of the polymer film, and C is its capacitance.

Energetics: The HOMO energy level of the neat films was measured by ambient photoemission spectroscopy (APS) with an APS04 from KP Technology. The Au tip was calibrated by calculating the absolute tip work function with respect to the vacuum using a Ag reference sample. The cube root of the photoemission signal was linearly fitted to calculate the HOMO of the sample and the mean of three measurements was taken.

Cyclic Voltammetry: Spectroelectrochemical measurements were measured of neat PQT12 on FTO coated glass substrates. A custom electrochemical cell was used with Pt counter electrode, Ag/AgCl reference electrode, and acetonitrile electrolyte (0.1 M $TBAPF_6$). Oxidizing potential was applied using an Autolab potentiostat PGSTAT101, CV sweep forward, and backward from −0.1 to 1.2 V at a scan rate of 0.02 V s^{-1}.

Raman Spectroscopy: A Renishaw inVia Raman microscope with InGaAs detector was used to collect Raman spectra and with a 50× objective in a backscattering configuration. Spectra were collected using a 785 nm diode laser at 9.0 mW power and the laser probe was defocused to ≈5 µm. Calibration of the filter and grating was performed using the well-defined 520 cm^{-1} peaks of a Si reference. For in situ field dependent Raman spectroscopy (EFDRS), the same Raman protocols were used. The sample was contained in Linkam HFS600E-PB4 sample chamber and a drain voltage applied across the source drain electrodes. A constant V_D was applied and held for 2 min before Raman measurements were taken; 20 positions down the 5 µm channel were probed at each applied voltage. In situ gas

© 2023 The Authors. Advanced Materials published by Wiley-VCH GmbH

15214095, 2024, 20, Downloaded from https://onlinelibrary.wiley.com/doi/10.1002/adma.202211184 by Imperial College London, Wiley Online Library on [17/06/2024]. See the Terms and Conditions (https://onlinelibrary.wiley.com/terms-and-conditions) on Wiley Online Library for rules of use; OA articles are governed by the applicable Creative Commons License

exposure under EFDRS was applied at high gas concentration in order to test analyze the changes in Raman signatures. The chamber was held under a N_2 flow of 1000 sccm and 0.2 mL was injected into chamber prior to the sample stage. The current was measured for the duration of gas exposure and Raman spectra taken at various points to probe the effects of gas exposure. This allowed measurement of the direction of current modulation and observation of vibrational mode changes but did not give a true indication of response time or concentration gradients.

DFT Simulation: Raman peak assignment and geometry analysis were simulated using density functional theory (DFT) on the Imperial College High-Performance Computing service using GAUSSAIN09 software.[85] All simulations were performed on single molecules in the gas phase using B3LYP level of theory and basis set 6–31G(d.p).[86–88] Oligomer length was simulated at 4, 8, 12, 16, and 20 thiophenes long with methyl side chains and 16T (tetramer of PQT12) was chosen as the base measurement due as the polaron delocalized along the full length of the simulated molecule at this length. The effect of side chains was investigated by simulating the 16T with no side chain, methyl, ethyl, propyl, and butyl side chains for P3HT and PQT12. Frequency of vibrations were identified from simulations of Raman spectra using empirical scaling factor of 0.97,[89] and peak assignments were visualized using GaussView 6.0.16 software. Geometry data and Hirshfeld charges were extracted from the optimization calculations of all 16T simulations and compared for the effect of side-chain density and length.

Supporting Information

Supporting Information is available from the Wiley Online Library or from the author.

Acknowledgements

The authors would like to acknowledge the UK EPSRC forfunding through both the ATIP Programme Grant (EP/T028513/1), and the Processable Electronics Centre for Doctoral Training (EP/L016702/1). This research was also supported by the UK Department for Business, Energy and Industrial Strategy (BEIS) through the National Measurement System and the Val O'Donoghue PhD Scholarship at Imperial College London. M.D. and S.E. acknowledge the EPSRC grant EP/S030727/1 for financial support.

Conflict of Interest

The authors declare no conflict of interest.

Data Availability Statement

The data that support the findings of this study are available from the corresponding author upon reasonable request.

Keywords

electrochemical doping, organic gas sensors, polaron formation, side-chain density, π-conjugated polymer

Received: November 30, 2022
Revised: June 16, 2023
Published online: September 17, 2023

[1] G. Hong, X. Gan, C. Leonhardt, Z. Zhang, J. Seibert, J. M. Busch, S. Bräse, *Adv. Mater.* **2021**, *33*, 2005630.
[2] F. M. van der Staaij, I. M. van Keulen, E. von Hauff, *Sol. RRL* **2021**, *5*, 2100167.
[3] S. Himmelberger, A. Salleo, *MRS Commun.* **2015**, *5*, 383.
[4] D. Zhi, E. Zhang, B. Zhang, F. Zhang, *Mol. Syst. Des. Eng.* **2022**, *7*, 553.
[5] M. Anderson, C. Ramanan, C. Fontanesi, A. Frick, S. Surana, D. Cheyns, M. Furno, T. Keller, S. Allard, U. Scherf, D. Beljonne, G. D'Avino, E. Von Hauff, E. Da Como, *Phys. Rev. Mater.* **2017**, *1*, 055604.
[6] C. Enengl, S. Enengl, S. Pluczyk, M. Havlicek, M. Lapkowski, H. Neugebauer, E. Ehrenfreund, *ChemPhysChem* **2016**, *17*, 3836.
[7] S. Fratini, M. Nikolka, A. Salleo, G. Schweicher, H. Sirringhaus, *Nat. Mater.* **2020**, *19*, 491.
[8] S. Kera, H. Yamane, N. Ueno, *Prog. Surf. Sci.* **2009**, *84*, 135.
[9] R. Steyrleuthner, Y. Zhang, L. Zhang, F. Kraffert, B. P. Cherniawski, R. Bittl, A. L. Briseno, J. L. Bredas, J. Behrends, *Phys. Chem. Chem. Phys.* **2017**, *19*, 3627.
[10] J. Nightingale, J. Wade, D. Moia, J. Nelson, J. S. Kim, *J. Phys. Chem. C* **2018**, *122*, 29129.
[11] M. Moser, A. Savva, K. Thorley, B. D. Paulsen, T. C. Hidalgo, D. Ohayon, H. Chen, A. Giovannitti, A. Marks, N. Gasparini, A. Wadsworth, J. Rivnay, S. Inal, I. McCulloch, *Angew. Chem., Int. Ed.* **2021**, *60*, 7777.
[12] J. Yamamoto, Y. Furukawa, *J. Phys. Chem. B* **2015**, *119*, 4788.
[13] S. Limbu, K. Stewart, J. Nightingale, H. Yan, C. Balamurugan, S. Hong, J. Kim, K. Lee, S. Kwon, J. S. Kim, *ACS Appl. Electron. Mater.* **2021**, *3*, 2152.
[14] S. Kwon, Y. Pak, B. Kim, B. Park, J. Kim, G. Kim, Y. R. Jo, S. Limbu, K. Stewart, H. Kim, B. J. Kim, S. Y. Jang, H. Kang, J. W. Min, J. S. Kim, G. Y. Jung, K. Lee, *J. Mater. Chem. A* **2020**, *8*, 16884.
[15] K. Stewart, S. Limbu, J. Nightingale, K. Pagano, B. Park, S. Hong, K. Lee, S. Kwon, J. S. Kim, *J. Mater. Chem. C* **2020**, *8*, 15268.
[16] J. D. Yuen, A. S. Dhoot, E. B. Namdas, N. E. Coates, M. Heeney, I. McCulloch, D. Moses, A. J. Heeger, *J. Am. Chem. Soc.* **2007**, *129*, 14367.
[17] D. Ofer, R. M. Crooks, M. S. Wrighton, *J. Am. Chem. Soc.* **1990**, *112*, 7869.
[18] I. Bargigia, L. R. Savagian, A. M. Österholm, J. R. Reynolds, C. Silva, *J. Am. Chem. Soc.* **2021**, *143*, 294.
[19] A. Marrocchi, D. Lanari, A. Facchetti, L. Vaccaro, *Energy Environ. Sci.* **2012**, *5*, 8457.
[20] A. Salleo, T. W. Chen, A. R. Völkel, Y. Wu, P. Liu, B. S. Ong, R. A. Street, *Phys. Rev. B* **2004**, *70*, 115311.
[21] R. K. Pandey, A. Kumar Singh, N. K. Singh, M. Rabelo, M. Ju, E.-C. Cho, R. Prakash, J. Yi, *Appl. Surf. Sci.* **2022**, *593*, 153413.
[22] M. K. Singh, A. Kumar, R. Prakash, *Mater. Sci. Eng., B* **2017**, *217*, 12.
[23] C. Kumar, G. Rawat, H. Kumar, Y. Kumar, R. Prakash, S. Jit, *IEEE Trans. Nanotechnol.* **2018**, *17*, 1111.
[24] C. Kumar, G. Rawat, H. Kumar, Y. Kumar, A. Kumar, R. Prakash, S. Jit, *IEEE Sens. J.* **2018**, *18*, 6085.
[25] A. V Marsh, M. Heeney, *Polym. J.* **2023**, *55*, 375.
[26] J. W. Jung, J. W. Jo, E. H. Jung, W. H. Jo, *Org. Electron.* **2016**, *31*, 149.
[27] S. Holliday, Y. Li, C. K. Luscombe, *Prog. Polym. Sci.* **2017**, *70*, 34.
[28] J. Lee, B.-L. Lee, J. H. Kim, S. Lee, S. Im, *Phys. Rev. B* **2012**, *85*, 045206.
[29] F. Bauch, C.-D. Dong, S. Schumacher, *RSC Adv.* **2022**, *12*, 13999.
[30] M. G. Voss, D. T. Scholes, J. R. Challa, B. J. Schwartz, *Faraday Discuss.* **2019**, *216*, 339.
[31] P. Pingel, A. Zen, D. Neher, I. Lieberwirth, G. Wegner, S. Allard, U. Scherf, *Appl. Phys. A: Mater. Sci. Process.* **2009**, *95*, 67.
[32] A. S. M. Tripathi, S. Sadakata, R. K. Gupta, S. Nagamatsu, Y. Ando, S. S. Pandey, *ACS Appl. Mater. Interfaces* **2019**, *11*, 28088.
[33] A. J. Heeger, S. Kivelson, J. R. Schrieffer, W. P. Su, *Rev. Mod. Phys.* **1988**, *60*, 781.
[34] J. S. Kim, S. Wood, S. Shoaee, S. J. Spencer, F. A. Castro, W. C. Tsoi, C. E. Murphy, M. Sim, K. Cho, J. R. Durrant, J. S. Kim, *J. Mater. Chem. C* **2015**, *3*, 9224.

© 2023 The Authors. Advanced Materials published by Wiley-VCH GmbH

15214095, 2024, 20, Downloaded from https://onlinelibrary.wiley.com/doi/10.1002/adma.202211184 by Imperial College London, Wiley Online Library on [17/06/2024]. See the Terms and Conditions (https://onlinelibrary.wiley.com/terms-and-conditions) on Wiley Online Library for rules of use; OA articles are governed by the applicable Creative Commons License

[35] A. N. Mallya, R. Kottokkaran, P. C. Ramamurthy, *Sens. Actuators, B* **2014**, *201*, 308.
[36] S. T. Keene, V. Gueskine, M. Berggren, G. G. Malliaras, K. Tybrandt, I. Zozoulenko, *Phys. Chem. Chem. Phys.* **2022**, *24*, 19144.
[37] S. B. Aziz, T. J. Woo, M. F. Z. Kadir, H. M. Ahmed, *J. Sci.: Adv. Mater. Devices* **2018**, *3*, 1.
[38] W. C. Tsoi, D. T. James, J. S. Kim, P. G. Nicholson, C. E. Murphy, D. D. C. Bradley, J. Nelson, J.-S. Kim, *J. Am. Chem. Soc.* **2011**, *133*, 9834.
[39] A. A. Virkar, S. Mannsfeld, Z. Bao, N. Stingelin, *Adv. Mater.* **2010**, *22*, 3857.
[40] R. Zhang, B. Li, M. C. Iovu, M. Jeffries-El, G. Sauvé, J. Cooper, S. Jia, S. Tristram-Nagle, D. M. Smilgies, D. N. Lambeth, R. D. McCullough, T. Kowalewski, *J. Am. Chem. Soc.* **2006**, *128*, 3480.
[41] J. F. Chang, J. Clark, N. Zhao, H. Sirringhaus, D. W. Breiby, J. W. Andreasen, M. M. Nielsen, M. Giles, M. Heeney, I. McCulloch, *Phys. Rev. B.* **2006**, *74*, 115318.
[42] F. P. V. Koch, J. Rivnay, S. Foster, C. Müller, J. M. Downing, E. Buchaca-Domingo, P. Westacott, L. Yu, M. Yuan, M. Baklar, Z. Fei, C. Luscombe, M. A. McLachlan, M. Heeney, G. Rumbles, C. Silva, A. Salleo, J. Nelson, P. Smith, N. Stingelin, *Prog. Polym. Sci.* **2013**, *38*, 1978.
[43] R. J. Kline, M. D. McGehee, E. N. Kadnikova, J. Liu, J. M. J. Fréchet, *Adv. Mater.* **2003**, *15*, 1519.
[44] R. J. Kline, M. D. McGehee, E. N. Kadnikova, J. Liu, J. M. J. J. Fréchet, M. F. Toney, *Macromolecules* **2005**, *38*, 3312.
[45] A. Zen, J. Pflaum, S. Hirschmann, W. Zhuang, F. Jaiser, U. Asawapirom, J. P. Rabe, U. Scherf, D. Neher, *Adv. Funct. Mater.* **2004**, *14*, 757.
[46] A. G. Dixon, R. Visvanathan, N. A. Clark, N. Stingelin, N. Kopidakis, S. E. Shaheen, *J. Polym. Sci., Part B: Polym. Phys.* **2018**, *56*, 31.
[47] G. De Luca, W. Pisula, D. Credgington, E. Treossi, O. Fenwick, G. M. Lazzerini, R. Dabirian, E. Orgiu, A. Liscio, V. Palermo, K. Müllen, F. Cacialli, P. Samorì, *Adv. Funct. Mater.* **2011**, *21*, 1279.
[48] C. M. Wolf, L. Guio, S. C. Scheiwiller, R. P. O'Hara, C. K. Luscombe, L. D. Pozzo, R. P. O'Hara, C. K. Luscombe, L. D. Pozzo, *Macromolecules* **2021**, *54*, 2960.
[49] C. Kumar, G. Rawat, H. Kumar, Y. Kumar, R. Prakash, S. Jit, *Org. Electron.* **2017**, *48*, 53.
[50] S. J. Kang, S. Song, C. Liu, D. Y. Kim, Y. Y. Noh, *Org. Electron.* **2014**, *15*, 1972.
[51] R. K. Pandey, A. K. Singh, R. Prakash, *J. Phys. Chem. C* **2014**, *118*, 22943.
[52] S. Limbu, Ph.D. thesis, Imperial College London, **2020**, https://doi.org/10.25560/86385.
[53] J. Luke, E. M. Speller, A. Wadsworth, M. F. Wyatt, S. Dimitrov, H. K. H. Lee, Z. Li, W. C. Tsoi, I. McCulloch, D. Bagnis, J. R. Durrant, J. S. Kim, *Adv. Energy Mater.* **2019**, *9*, 1803755.
[54] J. Clark, C. Silva, R. H. Friend, F. C. Spano, *Phys. Rev. Lett.* **2007**, *98*, 206406.
[55] W. Zhang, R. Hu, D. Li, M.-M. Huo, X.-C. Ai, J.-P. Zhang, *J. Phys. Chem. C* **2012**, *116*, 4298.
[56] H. Wang, J. Liu, Y. Xu, Y. Han, *J. Phys. Chem. B* **2013**, *117*, 5996.
[57] S. Limbu, K. B. Park, J. Wu, H. Cha, S. Yun, S. J. Lim, H. Yan, J. Luke, G. Ryu, C. J. Heo, S. Kim, Y. W. Jin, J. R. Durrant, J. S. Kim, *ACS Nano* **2021**, *15*, 1217.
[58] M. Makrygianni, A. Ainsebaa, M. Nagel, S. Sanaur, Y. S. Raptis, I. Zergioti, D. Tsamakis, *Appl. Surf. Sci.* **2016**, *390*, 823.
[59] E. Ditler, S. Luber, *WIREs Comput. Mol. Sci.* **2022**, *12*, e1605.
[60] J. L. Brédas, D. Beljonne, V. Coropceanu, J. Cornil, *Chem. Rev.* **2004**, *104*, 4971.
[61] C. R. Newman, C. D. Frisbie, D. A. Da Silva Filho, J. L. Brédas, P. C. Ewbank, K. R. Mann, *Chem. Mater.* **2004**, *16*, 4436.
[62] M. De Jong, L. Seijo, A. Meijerink, F. T. Rabouw, *Phys. Chem. Chem. Phys.* **2015**, *17*, 16959.
[63] J. E. Norton, J.-L. Brédas, *J. Am. Chem. Soc.* **2008**, *130*, 12377.
[64] G. R. Hutchison, M. A. Ratner, T. J. Marks, *J. Am. Chem. Soc.* **2005**, *127*, 2339.
[65] C. B. Gorman, S. R. Marder, *Proc. Natl. Acad. Sci. U. S. A.* **1993**, *90*, 11297.
[66] S. R. Marder, C. B. Gorman, B. G. Tiemann, J. W. Perry, G. Bourhill, K. Mansour, *Science* **1993**, *261*, 186.
[67] F. L. Hirshfeld, *Theor. Chim. Acta* **1977**, *44*, 129.
[68] K. B. Wiberg, P. R. Rablen, *J. Org. Chem.* **2018**, *83*, 15463.
[69] R. K. Hallani, B. D. Paulsen, A. J. Petty, R. Sheelamanthula, M. Moser, K. J. Thorley, W. Sohn, R. B. Rashid, A. Savva, S. Moro, J. P. Parker, O. Drury, M. Alsufyani, M. Neophytou, J. Kosco, S. Inal, G. Costantini, J. Rivnay, I. McCulloch, *J. Am. Chem. Soc.* **2021**, *143*, 11007.
[70] P. Hu, X. He, H. Jiang, *InfoMat* **2021**, *3*, 613.
[71] D. Natali, M. Caironi, *Adv. Mater.* **2012**, *24*, 1357.
[72] C. Liu, Y. Xu, Y. Y. Noh, *Mater. Today* **2015**, *18*, 79.
[73] N. A. Kukhta, A. Marks, C. K. Luscombe, *Chem. Rev.* **2022**, *122*, 4325.
[74] S. Wang, G. Zuo, J. Kim, H. Sirringhaus, *Prog. Polym. Sci.* **2022**, *129*, 101548.
[75] H. Li, M. E. Decoster, R. M. Ireland, J. Song, P. E. Hopkins, H. E. Katz, *J. Am. Chem. Soc.* **2017**, *139*, 11149.
[76] Y. Xuan, X. Liu, S. Desbief, P. Leclère, M. Fahlman, R. Lazzaroni, M. Berggren, J. Cornil, D. Emin, X. Crispin, *Phys. Rev. B* **2010**, *82*, 115454.
[77] T. O. Poehler, H. E. Katz, *Energy Environ. Sci.* **2012**, *5*, 8110.
[78] A. Lv, Y. Pan, L. Chi, *Sensors* **2017**, *17*, 213.
[79] B. Li, G. Sauvé, M. C. Iovu, M. Jeffries-El, R. Zhang, J. Cooper, S. Santhanam, L. Schultz, J. C. Revelli, A. G. Kusne, T. Kowalewski, J. L. Snyder, L. E. Weiss, G. K. Redder, R. D. McCullough, D. N. Lambeth, *Nano Lett.* **2006**, *6*, 1598.
[80] S. Mehrabani, A. J. Maker, A. M. Armani, *Sensors* **2014**, *14*, 5890.
[81] S. Jana, R. K. Pandey, R. Prakash, *ACS Appl. Polym. Mater.* **2022**, *4*, 4818.
[82] S. Agbolaghi, S. Zenoozi, *Org. Electron.* **2017**, *51*, 362.
[83] T. Ito, T. Shimomura, T. Miura, *J. Phys. Chem. B* **2017**, *121*, 1108.
[84] N. Siemons, D. Pearce, C. Cendra, H. Yu, S. M. Tuladhar, R. K. Hallani, R. Sheelamanthula, G. S. LeCroy, L. Siemons, A. J. P. White, I. McCulloch, A. Salleo, J. M. Frost, A. Giovannitti, J. Nelson, *Adv. Mater.* **2022**, *34*, 2204258.
[85] M. J. Frisch, G. W. Trucks, H. B. Schlegel, G. E. Scuseria, M. A. Robb, J. R. Cheeseman, G. Scalmani, V. Barone, G. A. Petersson, H. Nakatsuji, X. Li, M. Caricato, A. Marenich, J. Bloino, B. G. Janesko, R. Gomperts, B. Mennucci, H. P. Hratchian, J. V. Ortiz, A. F. Izmaylov, J. L. Sonnenberg, D. Williams-Young, F. Ding, F. Lipparini, F. Egidi, J. Goings, B. Peng, A. Petrone, T. Henderson, D. Ranasinghe, et al., *Gaussian 16, Revision C.01*, Gaussian, Inc., Wallingford, CT, USA **2016**.
[86] A. D. Becke, *J. Chem. Phys.* **1993**, *98*, 5648.
[87] G. A. Petersson, A. Bennett, T. G. Tensfeldt, M. A. Al-Laham, W. A. Shirley, J. Mantzaris, *J. Chem. Phys.* **1988**, *89*, 2193.
[88] P. J. Stephens, F. J. Devlin, C. F. Chabalowski, M. J. Frisch, *J. Phys. Chem.* **1994**, *98*, 11623.
[89] M. L. Laury, M. J. Carlson, A. K. Wilson, *J. Comput. Chem.* **2012**, *33*, 2380.

© 2023 The Authors. Advanced Materials published by Wiley-VCH GmbH

15214095, 2024, 20, Downloaded from https://onlinelibrary.wiley.com/doi/10.1002/adma.202211184 by Imperial College London, Wiley Online Library on [17/06/2024]. See the Terms and Conditions (https://onlinelibrary.wiley.com/terms-and-conditions) on Wiley Online Library for rules of use; OA articles are governed by the applicable Creative Commons License